

Measurement setup for the characterization of integrated semiconductor circuits at cryogenic temperatures

Cite as: Rev. Sci. Instrum. 96, 044701 (2025); doi: 10.1063/5.0245525

Submitted: 27 October 2024 • Accepted: 10 March 2025 •

Published Online: 1 April 2025



View Online



Export Citation



CrossMark

P. J. Ritter,^{1,a)} M.-A. Tucholke,¹ M. Neumann,¹ J. F. Mumme,¹ A. Meyer,² R. Roederer,³ Z. Guo,² A. Pawlak,³ V. Issakov,² M. Schilling,¹ and B. Hampel¹

AFFILIATIONS

¹ Institut für Elektrische Messtechnik und Grundlagen der Elektrotechnik, TU Braunschweig, 38106 Braunschweig, Germany

² Institut für CMOS Design, TU Braunschweig, 38106 Braunschweig, Germany

³ Infineon Technologies AG, 85579 Neubiberg, Germany

^{a)} Author to whom correspondence should be addressed: p.ritter@tu-braunschweig.de

ABSTRACT

Integrated semiconductor circuits operating at cryogenic temperatures can play a crucial role in scaling quantum computing architectures based on trapped-ion and superconducting qubits. Other technologies, such as low-temperature detectors, can also benefit significantly from these circuits. These applications demand high-frequency, cryogenic temperature measurement systems for the thorough characterization of semiconductor components and circuits. This work presents a customizable, high-frequency, fast, and reliable cryogenic measurement setup for measurement temperatures ranging from room temperature to 4.2 K. It features up to two dc probes or two ground-signal-ground probes for frequencies of up to 67 GHz, which can be configured in a 180° or 90° configuration. In addition, up to 48 BeCu wires configured as twisted pairs provide supply and control signals. Furthermore, up to four rf connections can be mounted directly to a printed circuit board. The setup features an optical microscope in the vacuum chamber to position the probes, which is further utilized by a machine vision algorithm, allowing the detection of pads and automatic positioning of the probes over the pads. The hardware is located in a 550 × 500 × 500 mm³ large vacuum chamber with two independent pulse tube cryocoolers with cooling powers of up to 0.9 and 0.4 W at 4.2 K. Exemplary room temperature and cryogenic S-parameter, transient frequency (f_T), time-domain, capacitance–voltage, and dc measurements of single transistors and integrated circuits fabricated by *Infineon* are presented, demonstrating the system's measurement capability for quantum computing and other applications.

© 2025 Author(s). All article content, except where otherwise noted, is licensed under a Creative Commons Attribution (CC BY) license (<https://creativecommons.org/licenses/by/4.0/>). <https://doi.org/10.1063/5.0245525>

I. INTRODUCTION

The characterization of semiconductor circuits at very low temperatures gains new importance as the interest in operating integrated circuits (ICs) at cryogenic temperatures for quantum computer (QC) applications is growing extensively. While many QC experiments are based on superconducting circuits with Josephson junctions, several research groups and companies worldwide develop quantum computers based on trapped ions that offer much longer coherence times,¹ high fidelity, and higher operation temperatures.² One approach to scale these technologies to larger qubit

numbers requires greater integration of control and supply signals close to the quantum computing chip. Such signals can efficiently be provided by semiconductor circuits that are integrated into the quantum computing chip itself, into its interposer, or in a separate chip close to the quantum computing chip.^{3–5} Therefore, integrated circuits would need to operate at cryogenic temperatures, and their power dissipation must be very low to preserve the available cooling power. Designing such complex systems necessitates the characterization and modeling of individual device components.^{6–8} This work introduces a measurement setup that effectively contributes to the characterization process.

The measurement setup presented here offers a unique combination of flexibility and automation compared to commercially available solutions. Highly automated setups designed for high throughput production use exist, such as the commercial *Form-Factor* HPD IQ3000^{9,10} probing station. It operates on full wafers down to 4 K and supports a large number of probes up to 18 GHz; however, they are rigidly mounted to a common frame and cannot be moved relative to each other while in use, thereby severely limiting flexibility. Probing stations targeting research applications are more flexible; however, they are usually manually actuated and, thus, lack the capabilities required for automation. The PSCC system by *Advanced Research Systems*¹¹ can measure at up to 67 GHz down to 4 K. *Lake Shore Cryotronics, Inc.* offers comparable systems.¹² More specialized setups¹³ exist for reaching higher frequencies of up to 116 GHz at 19 K using waveguides; however, their associated cost is higher and at the expense of higher temperatures. While many probing stations are operated in a closed-cycle, there are systems employing open-cycle coolers.¹⁴ However, such coolers' operating costs are considerably higher, making pulse tube closed-cycle cryocoolers the preferred option in most cases.

The setup presented in this work allows the independent movement of multiple probes and the possibility of simultaneous bonded connections. Such high versatility provides great advantages in the context of research applications with varying devices under tests (DUTs). The added capability of semi-automated movement significantly reduces human operation time for characterizing multiple devices on the same chip, a process typically spanning several days. The maximum frequency of 67 GHz strikes a good balance of capability vs complexity and cost and generally suffices for the modeling of transistors. Some QC approaches require higher frequencies for the operating electronics than the actual control signals.¹⁵

This work presents an expansion on the functionalities of the established THz microscope in the Laboratory for Emerging Nanometrology (LENA) at TU Braunschweig.¹⁶ The THz microscope was developed for contactless measurements of high-frequency electromagnetic fields from 1 GHz to 5 THz using a high-temperature superconducting sensor,^{17,18} a so-called Josephson cantilever. A new measurement mode employing contacting probes has been implemented within the scope of this work to facilitate traditional galvanic measurement of the electrical properties of DUTs. Using two ground-signal-ground (GSG) probes enables the measurement of two-port S-parameters with frequencies of up to 67 GHz. The probes are designed to be positioned in either a facing (opposing) or an orthogonal (90°) orientation. Simultaneously, up to 48 dc connections can be bonded to the chip. One or both GSG probes can be replaced by dc probes with up to 12 dc contacts each. These features enable the setup to measure a wide variety of integrated circuits. Furthermore, measurements with a combination of the Josephson cantilever and one probe are also possible. This capability could be particularly useful for characterizing THz sources, which are driven by dc or GHz input signals. Examples are monolithic microwave integrated circuits (MMICs) or quantum cascade lasers (QCLs), which require cryogenic operation.

This paper introduces the measurement chamber (Sec. II A) and its critical components for galvanic probe measurements,

including the optical microscope (Sec. II B), vibration-isolated chuck (Sec. II C), cryogenic shielding (Sec. II D), and probes (Sec. II E), along with the final operating temperatures (Sec. II F). In the following section, we introduce the software for the automated measurement routines (Sec. III A) and software features of the optical microscope (Sec. III B), such as semi-automated prober placement using machine vision. Finally, measurement examples (Sec. IV) are provided, covering a range from dc (Sec. IV A) to capacitive (Sec. IV C) and S-parameter measurements (Sec. IV D), as well as measurements of integrated semiconductor circuits (Secs. IV B and IV E).

II. CRYOGENIC MEASUREMENT SETUP

This section introduces the measurement setup for the cryogenic characterization of semiconductor circuits. The measurement chamber (Sec. II A) contains an optical microscope (Sec. II B) and a vibration-isolated chuck (Sec. II C). It is equipped with appropriate shielding (Sec. II D), and several probes are available for different measurement tasks (Sec. II E). Finally, the achievable cryogenic temperatures are characterized, and key parameters are summarized (Sec. II F).

A. Measurement chamber

Cryogenic measurements of electronics can only be performed in a vacuum chamber for thermal insulation. The chamber in this setup has a volume of $550 \times 500 \times 500 \text{ mm}^3$ and has two doors for easy accessibility, which is shown in Fig. 3(I), and multiple optical access ports. The vacuum is created with a turbo molecular pump, which is assisted by a rotary valve pump. The chamber is evacuated to a pressure of less than $5 \times 10^{-5} \text{ mbar}$ before engaging the pulse tube cryocoolers.¹⁶ The vacuum insulates the cold parts from the rest of the chamber so that electronics at room temperature, such as the readout electronics of the optical microscope, can be installed inside the vacuum chamber. The measurement setup employs two pulse tube cryocoolers from *Sumitomo Heavy Industries, Ltd.* The first cryocooler, RP-082B2S, with a cooling power of 0.9 W at 4.2 K, is used to cool the sample, while the second cryocooler, RP-062BS, with a cooling power of 0.4 W at 4.2 K, cools the rf cables, which connect the probes to the measurement device. The thermalization of the rf cables is performed on the second cryocooler since this method reduces the overall cable length. The first stages of both cryocoolers reach $\sim 30 \text{ K}$, while the second stages operate at a nominal temperature of 4.2 K. The positioning systems of the probes have to be maintained close to room temperature. This is achieved through polyetheretherketone (PEEK) mounts, which increase thermal resistance, and the cold parts are thermally anchored with copper braids. Such a probe mount is depicted in Fig. 2(b) and schematically in Fig. 3(II). One of the two probe mounts is attached to a three-axis piezo-positioning system from the SLC-24 series by *SmarAct GmbH*. This allows the probe to be positioned within a volume of $50 \times 50 \times 16 \text{ mm}^3$. The other probe is attached to another SLC-24 series piezo-positioning system, which allows it to cover an even larger volume of $120 \times 120 \times 35 \text{ mm}^3$.

B. Optical microscope

Positioning the probes on the sample requires an optical microscope inside the vacuum chamber. The microscope from *Seed Studio* is depicted in Fig. 1. It is equipped with an additional Barlow lens to achieve a working distance between 48.5 and 33.5 mm for magnifications between 0.7 and 4.5 with an effective field of view between 9.81×7.4 and 1.39×1.05 mm². The image sensor *Sony IMX477* is controlled by the Arducam Module RB-Adu-174 to connect the microscope as a USB video device class (UVC). The optical microscope can be positioned using three linear stages (M112) from *Physik Instrumente*, each with a travel range of 25 mm. Homogeneous illumination is achieved by using light-emitting diodes (LEDs) that have a small viewing angle of 25° to minimize stray light. The zoom of the microscope can be adjusted with a servo motor.

C. Vibration isolated chuck

The second stage of pulse tube cryocoolers typically vibrates 14 μm peak-to-peak¹⁹ due to large helium pressure oscillations within the cold stages.²⁰ While this is better than Gifford–McMahon cold heads,²⁰ both systems are insufficiently damped to safely and repeatably position probes on the pads of a sample. The vibration not only accelerates the deterioration of the probes but also damages the pads of the sample. Therefore, vibrations have to be minimized. For this purpose, a braided oxygen-free (OF) copper cable was used to connect the chuck to the cold head. This assembly is depicted in Fig. 2(a) and includes an adapter made from oxygen-free high thermal conductivity (OFHC) copper to connect the cold head to the copper braid. The joints between the copper braid and both the cold head adapter and the chuck were cold pressed to ensure a good thermal connection.²¹ The sample chuck is designed to facilitate the mounting of samples and to thermalize the probes. It was fabricated from OFHC copper with a diameter of 75 mm and an effective sample area of 25×25 mm². The sample holder shown in Fig. 2(c) consists of two OFHC copper parts and facilitates the swap of samples. A calibration substrate can be mounted on one part and a DUT on the other. This allows for changing only the sample, reducing the risk of damaging the calibration substrate. The chips are mounted

TABLE I. Vibrations in the x, y, z directions of the sample chuck caused by the probe cryocooler (attached to the sample chuck), the sensor cryocooler (where the rf cables are thermalized), or both cryocoolers. The highest peak-to-peak vibrations Max_{PP} of one swing and the average peak-to-peak vibrations $Average_{PP}$ are shown.

	Max_{PP} (μm)	$Average_{PP}$ (μm)
X—only probe cryocooler	1.460	1.434
X—only sensor cryocooler	0.248	0.211
X—both cryocoolers	1.464	1.180
Y—only probe cryocooler	0.752	0.726
Y—only sensor cryocooler	0.524	0.398
Y—both cryocoolers	0.999	0.603
Z—only probe cryocooler	0.186	0.178
Z—only sensor cryocooler	0.085	0.077
Z—both cryocoolers	0.261	0.210

using conductive silver, which can easily be removed with acetone. Indium solder is another well-suited method; however, the sample must be heated.

To ensure accurate measurements, it is essential to thermalize the probes to the same temperature as the DUT. This prevents thermal contraction of the probes when touched down on the DUT, which could otherwise lead to connection loss between the probe tips and pads. This is particularly problematic when performing S-parameter measurements at high frequencies where the touch-down pressure needs to be uniform and repeatable. The touch-down pressure is monitored by observing the overtravel of the probe tips. In addition, the sample will be heated if there is a temperature gradient from the probe to the sample. To mitigate this issue, the probes are thermally anchored to the sample chuck as shown in Fig. 2(b). The temperature difference between the sample chuck and probe is now only 4.5 K at the lowest achievable temperature. The maneuverability of the probes is not compromised because flexible copper braids are employed to connect the probe mount to the bracket for mounting on the sample chuck [Fig. 2(b)]. In addition, the copper braid is wrapped with multi-layer insulation foil. The copper probe mount is screwed on a PEEK mount, which is also wrapped in multi-layer insulation foil and connected with PEEK screws to a copper shield as shown in Fig. 2(b). This copper shield is connected by another flexible copper braid to the chuck shield [Fig. 2(d)].

The vibrations of the sample chuck were characterized when either or both of the two cryocoolers were operated. They were measured with a white light interferometer *IMS5400-DS19* from *Micro-Epsilon Messtechnik* that was mounted to the baseplate of the vacuum chamber with the help of optical posts and accessories. The measurement results are shown in Table I. The highest peak-to-peak vibration amplitude was measured to be 1.464 μm in the x-direction of the probes. The maximum vibration in the y-direction has a peak-to-peak amplitude of 0.999 μm, while the largest vibration in the z-direction was measured to be only 261 nm. These results show a sufficient reduction of vibrations due to the outlined vibration isolation measures. The significant difference between the Max_{PP} and $Average_{PP}$ can be attributed to interference caused by the different pulse frequencies of the cryocoolers.

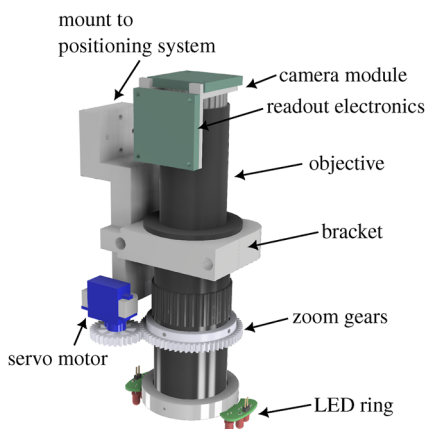


FIG. 1. CAD design of the optical microscope.

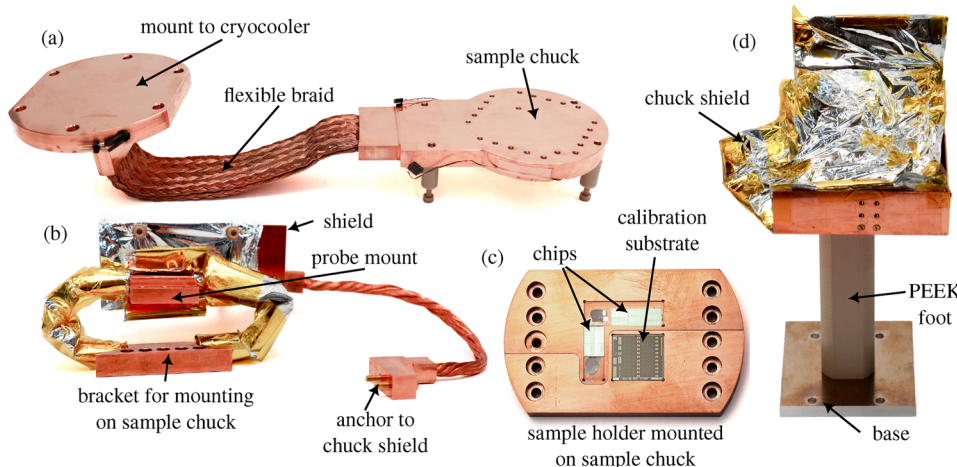


FIG. 2. Parts of the vibration isolated sample chuck. (a) Cold head to chuck assembly, (b) probe mount with thermal anchoring and shield, (c) sample holder from OFHC, and (d) chuck thermal shield with PEEK foot and aluminum base. The sample chuck is usually mounted in the middle of the chuck shield as shown in Fig. 3(III).

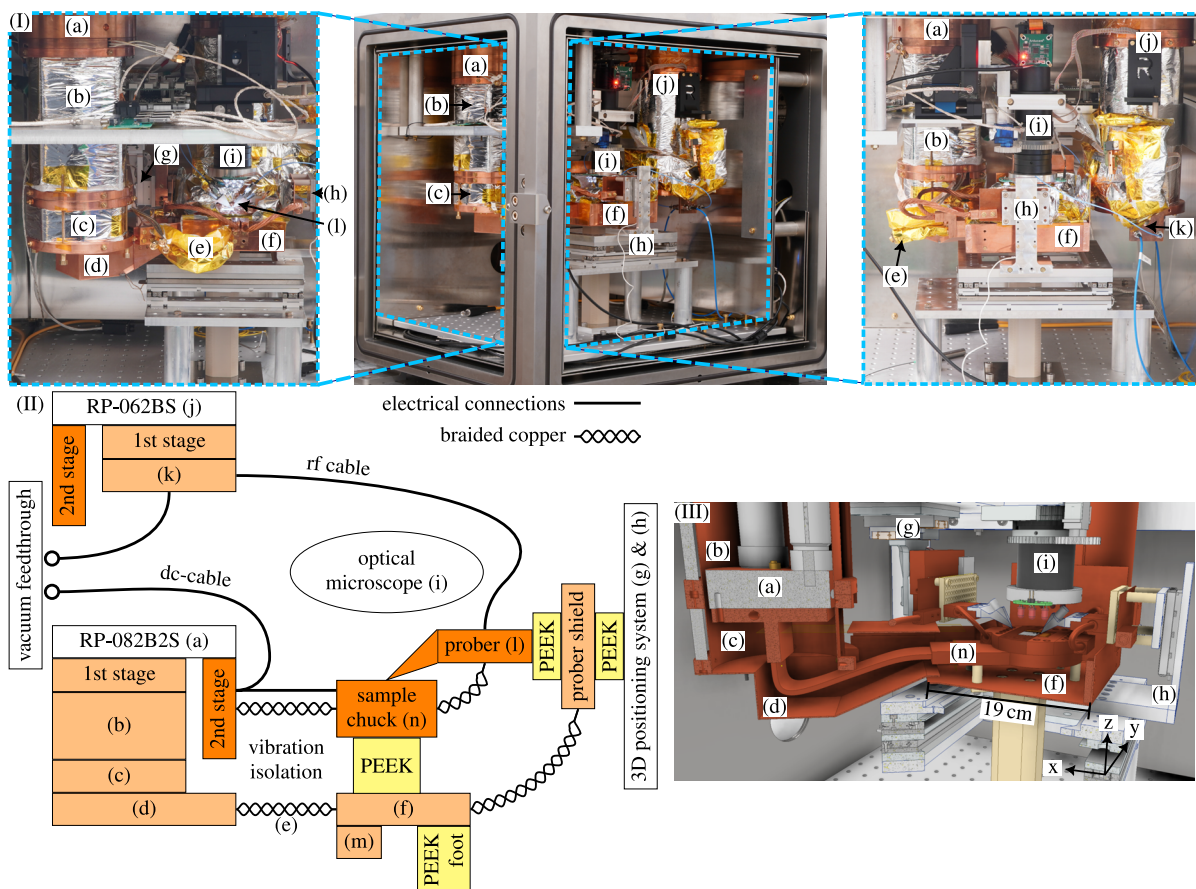


FIG. 3. Overview of the measurement chamber and annotated parts. Panel (I) shows different perspectives of the chamber, panel (II) shows a schematic overview of all annotated parts, and panel (III) is a detailed schematic of the shield layout for the DUT cooler. In panel (II), the parts are color-coded by temperature: orange for connections to the second stage (≈ 4 K), light orange for the shields (≈ 30 K), yellow for the temperature isolation, and white for the room temperature. (a) Cryocooler RP-082B2S, (b) fixed first stage shield, (c) first stage shield extension, (d) first stage shield for flexible copper braid to chuck, (e) connection between (d) and (f), (f) shield of sample chuck as in Fig. 2(d), (g) positioning system SLC-24 series prober 1, (h) positioning system SLC-24 series prober 2, (i) optical microscope, (j) cryocooler RP-062BS, (k) thermal mount for cables on the first stage of (j), (l) probes, (m) optional L-shaped shield, and (n) sample chuck.

D. Shielding

The shielding of the 4 K stage is critical due to the large amount of blackbody radiation caused by the vacuum chamber itself, resulting in thermal heat-up of the 4 K stage. The heat transfer due to radiation scales with the difference of the fourth power of the temperature between the object (T_1) and its surroundings (T_2) according to the Stefan–Boltzmann Law [Eq. (1)], where P is the net radiated power, σ is the Stefan–Boltzmann constant, ϵ is the emissivity of the object, and A is the surface area of the object,

$$P = \sigma\epsilon A(T_1^4 - T_2^4). \quad (1)$$

Even for a small round surface area at 4 K like the surface of the sample chuck with a diameter of 75 mm and a very good emissivity of $\epsilon_{\text{copper}} = 0.1$, which can be achieved by polishing the copper, the total heat flow is around $P = 0.2$ W to the sample chuck when it is exposed to blackbody radiation from the vacuum chamber with a temperature of 300 K. This represents a large fraction of the available cooling power at 4.2 K.

Therefore, thermal shields are required and were installed as depicted in Figs. 3(b)–3(d) and 3(f). Multiple shields are used to allow for a flexible design and easy handling. The first shield [Fig. 3(b)] is mounted directly to the cryocooler and has a cylindrical shape, which reaches the base of the cryocooler. It is also wrapped in multi-layer insulation foil to increase the reflectivity. The next shield [Fig. 3(c)] is used as a spacer but is very similar to the first one. The shield one after that [Fig. 3(d)] covers the mount to the cryocooler and flexible copper braid of Fig. 2(a). The following shield is not directly connected to the previous shield in order to mitigate vibrational coupling. This chuck shield [Fig. 3(f)] is the same as shown in Fig. 2(d) and is only connected to the other shield with two flexible copper braids [Fig. 3(e)]. It is mounted on a PEEK foot as shown in Fig. 2(d) and fastened to the base of the chamber. Therefore, vibration is minimized between the shields. The aforementioned shields of the probes in Sec. II C are also connected to the chuck shield via further flexible copper braids. The chuck shield encloses the sample chuck [Fig. 2(a)], which is mounted to the chuck shield with PEEK spacers and PEEK screws. The chuck shield only shields the bottom and one side of the sample chuck since a fully enclosed thermal shield is not feasible due to the proximity of the piezo-positioning systems and the optical microscope, both of which must remain close to room temperature. Finally, an L-shaped shield [Fig. 3(m)] can be used to cover the top and remaining sides of the sample chuck. The thermal shields are fabricated from OF copper as the thermal conductivity is sufficient at temperatures above 30 K.

E. Probes

The utilized probes are from the $|Z|$ and Multi- $|Z|$ series by *FormFactor Inc.*, which are suitable for cryogenic temperatures. An arbitrary combination of two different probe types can be installed in a facing (opposing) or an orthogonal (90°) orientation, as shown in Fig. 4(b). Ground-signal-ground (GSG) $|Z|$ probes with a pitch of 100 μm can be used for S-parameter measurements [Fig. 4(a)]. They are characterized up to a frequency of 67 GHz and connected to the measurement electronics by 1.85 mm connectors, a combination of flexible 0.047 and 0.085 inch coaxial cables, and a

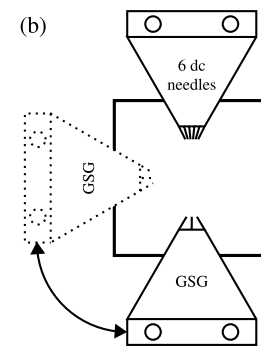


FIG. 4. (a) Installed GSG probes in an opposing configuration, contacting a chip; and (b) schematic orientation of the probes in a facing (opposing) or orthogonal (90°) orientation.

1.85 mm hermetic vacuum feedthrough. The off-the-shelf 0.047 inch coaxial cables had to be modified to increase their durability over multiple cooldown cycles. The inner conductor of the cables was soldered to the center pin of the 1.85 mm connector instead of a press fit. The rf cables are thermally anchored to the first stage of the second cryocooler, RP-062BS, to reduce the thermal load on the probes [Fig. 3(k)].

In this case, the Multi- $|Z|$ probes have six needles with a pitch of 100 μm and can be used for dc and low-frequency measurements. Each Multi- $|Z|$ probe is connected to the room temperature measurement electronics by one of two installed BeCu cryoloom cables from *CMR-Direct*, each featuring 12 twisted pairs for a total of 48 BeCu connections. This enables four-terminal measurements directly at the connector of the Multi- $|Z|$ probes using an adapter printed circuit board (PCB). The capacitance of a twisted pair within the cryoloom measures 200 pF, as determined by evaluating the entire cable length to the measurement instrument. It can be substantially decreased to 30 pF when utilizing the most distant cable strands in the cryoloom. The dc resistance of one cable strand is $\approx 4 \Omega$ at room temperature and decreases toward lower temperatures. In comparison to other systems that reported capacitive loads of 480 pF,²² 400 pF,²³ and 100 pF,²⁴ our system shows a favorable comparison.

F. Key parameters

The final reachable temperatures of the samples depend on the installed number of probes. Each probe adds additional surface area, which increases the radiation heat transfer. The mount of

TABLE II. List of reachable temperatures. Column (a) is the configuration as shown in Figs. 3(I), 3(II), and 4(a), but without any installed probes; column (b) is exactly as shown in Figs. 3(I), 3(II), and 4(a); column (c) is only one Multi-|Z| probe instead of 2 GSG probes; column (d) is the final temperature when the chuck is mounted directly on the second stage of the RP-082B2S cryocooler and enclosed by a shield; and column (e) is same as (d) but with 48 BeCu wires and three rf connections connected and operating IC ($P \approx 24$ mW).

Sensor	(a) No probes (K)	(b) 2 × GSG probes (K)	(c) 1 × dc probe (K)	(d) Under second stage (K)	(e) Under second stage cables (K)
First stage	29.28	39.23	33.71	29.49	32.24
Second stage	3.70	5.21	4.88	2.81	3.59
Chuck	7.09	11.93	10.93	3.60	4.20

TABLE III. Cryogenic specifications of only the probe setup.

Parameter	Specification
Cool down time to 15 K	2 h 45 min
Heat up time to 300 K	2 h 40 min
Lowest chuck temperature	10.93 K
Continuous chuck temperatures	300 K; 200–11 K
Max sampling area	25 × 25 mm ²
Frequency range	DC - 67 GHz

each probe consists of PEEK spacers and a copper shield to minimize the thermal loading. However, every contact joint to higher temperature parts impacts the final temperature negatively. Additional shields can be used to improve the cooling performance when only one or no probes are used. If the DUT is wire-bonded and no probes are required, it can be mounted directly on the second stage of the cryocooler RP-082B2S and fully enclosed by a shield. This minimal configuration consists of a PCB to which the sample is wire-bonded and connected to a cryoloop cable. This yields the lowest DUT temperature of 3.6 K. When all three SMA cables and both cryoloops are connected to a PCB, which is mounted under the second stage, the temperature increases to 4.2 K as shown in Table II(e). An overview of different measurement configurations is presented in Table II. Calibrated temperature sensors from *Lake Shore Cryotronics, Inc.* are used to measure the temperature of the second stage and chuck, while the first stage uses an uncalibrated sensor. Table III shows key parameters of the cryogenic measurement setup.

III. SOFTWARE

The automation of the setup greatly relies on the software. Section III A describes the automation of the measurement tools using LabVIEW, while Sec. III B covers the software for the optical microscope and the semi-automated probe positioning system.

A. Automated measurements

The measurement setup is controlled using an embedded controller (PXIe-8840) for the PXI system from *National Instruments* (NI). A GUI was programmed in LabVIEW to control all measurement devices. The measurement devices are located outside of the

chamber at room temperature and can be connected as needed. These include a vector network analyzer (VNA) Keysight E8361a, up to three source-measure units (SMUs) Keithley 2450, a lock-in amplifier MFLI from *Zurich Instruments*, an oscilloscope, and other digital outputs from the NI PXIE-6363 card. The devices can be programmed to record measurement data synchronously according to a given configuration file. This file configures all measurement devices to the desired settings and can be executed manually or triggered by an event. Events can be defined as occurring either after reaching a certain temperature or after a specified time, allowing automated temperature sweep measurements of devices.

B. Optical microscope

The optical microscope is controlled by a custom *Python* program that also allows the positioning of the probes. A live image from the optical microscope is displayed at all times to allow manual verification of the probe's positions.

In addition, machine vision algorithms are available to allow for faster navigation of the probes and the optical microscope. An autofocus algorithm was implemented, using the sum-modified Laplacian (SML),²⁵ to yield sharp images by moving the optical microscope.

Furthermore, an algorithm based on direct image stitching²⁶ was developed to create a panoramic image. This feature allows for quick and precise positioning of the optical microscope and the probes over the whole area of the sample. The position of the probes and the microscope from the pixels of the panorama is calculated using a homography matrix.²⁷

The calculation of these matrices requires a calibration of the probe's positions. Therefore, the probe positions in the microscope images are detected using a two-step process. In the first step, the general region of interest (ROI) is calculated using the Laplacian operator and subsequent max pooling.²⁸ This ROI is extracted and processed in the second step, which locates the precise position of the tips of the probe using adaptive thresholding and fitting a line through the detected shapes. The extraction of the ROI reduces the processing time and the probability of faulty probe tip detections. Figure 5 shows the results of the probe detection process. The red-framed part depicts the identified ROI, and the detected tips are marked with red circles in the magnified inset. In tests with 3000 images, the probe location detection algorithm correctly identified the probe's position in 85.62% of cases when it was close to the center of the image. However, when the probe was positioned off-center, the success rate dropped to 70.22%,

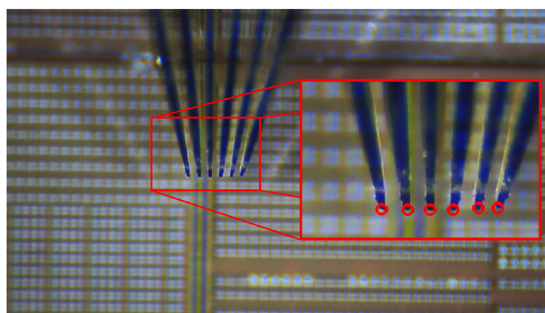


FIG. 5. Detection of the tips of a dc probe.

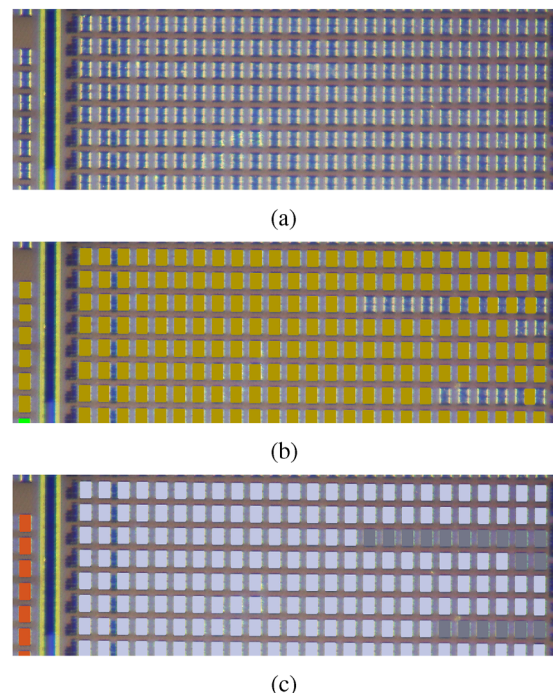
TABLE IV. Accuracy of the pad detection in 60 single images with 40 137 contact pads.

	Correlation only	Correlation and correction
Correctly detected pads	33 593 (83.70%)	38 270 (95.35%)
False positives	2454 (6.11%)	1357 (3.38%)
Undetected pads	6544 (16.30%)	1867 (4.65%)

likely due to distortions caused by camera lens aberrations. The image background significantly impacts the detection rate. Usually, after a small movement of the probe, the tips are detected correctly.

Another feature of the optical microscope software is the detection of contact pads of electrical devices in the panorama image as well as in single images. The position of contacts is found via cross correlation, which detects 83.7% of the contact pads (see Table IV). The results of the correlation are then corrected by considering the relative positions and sizes of the pads, increasing the detection rate to 95.3% and reducing the number of hallucinated contact pads by 44.7% (see Table IV). Figure 6(a) shows a part of an image where the contacts are to be detected. Figure 6(b) shows the detected contacts after the correlation. Noticeably on the right side, some contacts could not be detected and some were hallucinated. In Fig. 6(c), the results of the interpolation and elimination are shown, and the interpolated contacts are depicted in a darker color. This procedure is a robust way to detect pads, even when there are incomplete pad rows, paving the way toward fully automated measurements, where the probes automatically touch the pads.

A semi-automatic control of the probes and the optical microscope is achieved as the probe and optical microscope can be automatically moved to the position of a detected pad. Controlling the probes and optical microscope with this feature is much faster and less prone to errors than moving them manually. After the calibration process of the probes, their offset is usually well within 50 μm and can be compensated in software. The offset is constant over the entire chip, and the semi-automatic positioning is repeatable and precise enough to immediately initiate the touchdown process after the movement.

**FIG. 6.** Detection and interpolation of electrical contacts. (a) Extract of an original image. (b) Contacts found with correlation. (c) Interpolated contacts.

IV. MEASUREMENTS

The design of integrated cryogenic electronics requires accurate models of semiconductor devices within a foundry process design kit (PDK) to allow for precise simulation of complex, integrated circuits. However, PDKs are typically only characterized within a limited temperature range, usually between -40 and 125°C , as this meets the standard requirements of the industry. Yet, semiconductor properties can drastically change at cryogenic temperatures, potentially leading to unanticipated behavior or malfunction.^{29–31} Hence, precise models of passive components, such as resistors and capacitors, and active components, such as transistors, have to be created and verified with measurements at cryogenic temperatures. Finally, integrated circuits need to be tested to verify all components' functional interaction.

With the setup introduced in this work, various measurement types for the characterization of semiconductor components can be performed, including dc current and voltage measurements, voltage-dependent capacitance measurements, two-port S-parameter measurements, and time-resolved measurements of active circuits. All measurements can be executed at room temperatures and cryogenic temperatures as low as 3.6 K, enabling full PDK characterization. Subsequently, a selection of relevant measurements for integrated quantum computer electronics is presented in Secs. IV A–IV E, with the devices fabricated by Infineon.

A. dc measurements

The static analysis of circuits is often necessary to determine the functionality of a DUT. A basic example is the measurement of a

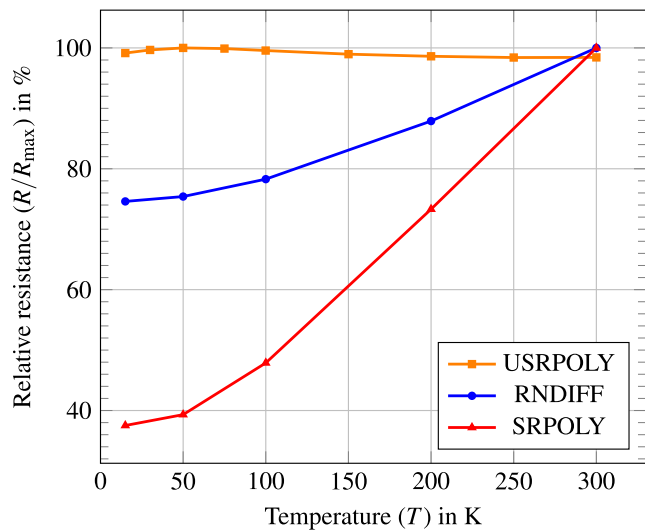


FIG. 7. Relative resistance vs temperature of single device resistors measured with one dc probe as outlined in Table II(c).

resistor's resistivity. A fixed current is applied to the resistor, and the voltage drop across it is measured. A four-terminal measurement must be performed to exclude the resistance of the wires. This was done directly on the chip, which is the most accurate method as it also excludes the probe's contact resistance. Figure 7 shows the temperature-dependent measurements of three different types of resistors from Infineon. Un-salicid poly-silicon (USRPOLY) resistors exhibit only a small change in resistivity over temperature, with their maximum resistance occurring at around 50 K. In contrast, n-diffusion resistors (RNDIFF) and salicid poly-silicon (SRPOLY) resistors show a drastic decrease in resistivity with temperature,

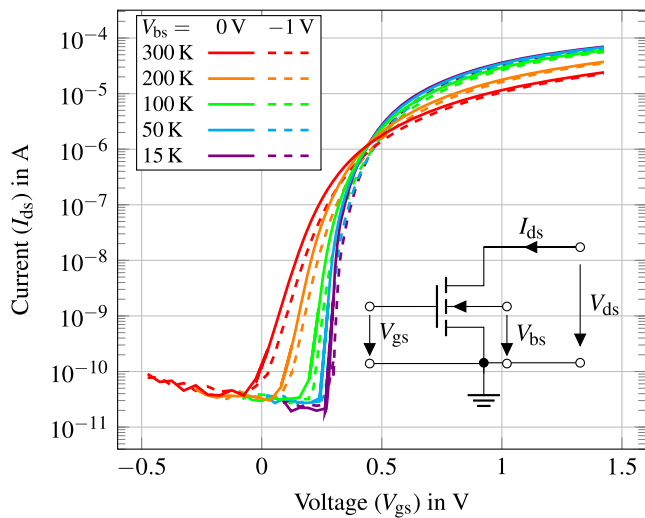


FIG. 8. Temperature dependent I - V curve of an n-channel MOSFET at $V_{bs} = 0, -1$ V, and the same $V_{ds} = 1.3$ V. The device has a width of 1 μm and a length of 10 μm . The device was measured with one dc probe as outlined in Table II(c).

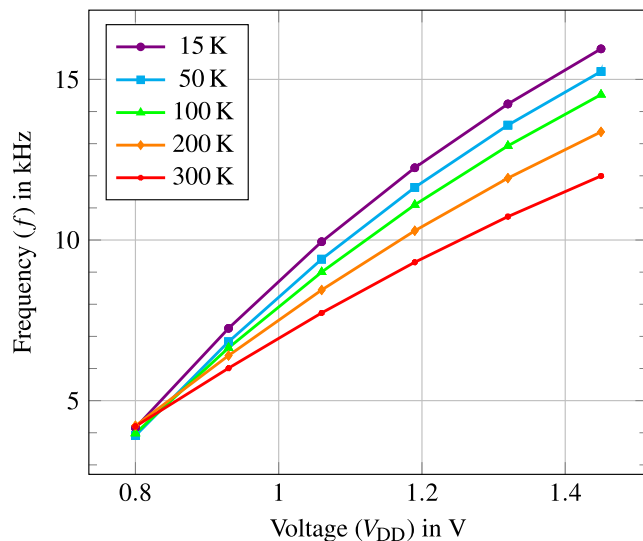


FIG. 9. Temperature dependent ring oscillator measurements with the same supply voltage (V_{DD}) sweep. The device is realized as a 49 stage single-finger inverter ring oscillator, using devices with the minimum length of the technology. The device was measured with one dc probe as outlined in Table II(c).

which agrees with the findings in Ref. 32. Such results emphasize the importance of cryogenic characterization, given that RNDIFF and SRPOLY resistors can exhibit dramatically different behaviors at cryogenic temperatures, posing considerable risks for integrated chip designs.

Another type of dc characterization involves measuring transistors. The I - V characteristics of a metal-oxide-semiconductor field-effect transistor (MOSFET) are crucial for understanding and designing circuits that use these types of transistors. One characterization step involves sweeping the gate voltage V_{gs} while the drain voltage V_{ds} is fixed and measuring the drain current I_{ds} . An exemplary measurement of such a sweep for an NMOS transistor is shown in Fig. 8. Compared to room temperature, a noticeable increase in the transistor's threshold voltage is noticed while the transistor's sub-threshold slope is also increasing. This measurement is in good agreement with the results gathered in Refs. 33 and 34.

B. Ring oscillators

The gate delay of MOSFETs can be investigated by studying the oscillation frequency of ring oscillators (ROs) placed on-chip. ROs are realized by placing several (N) inverters in series with each inverter causing a fixed delay t_{delay} , where the RO's output frequency can be calculated according to

$$f_{\text{RO}} = \frac{1}{2 \cdot N \cdot t_{\text{delay}}} \quad (2)$$

As the inverter's delay depends on the transistor's intrinsic parameters, such as its threshold voltage or mobility, it is heavily affected by a change in temperature.

Consequently, our setup was utilized to investigate the RO's oscillation frequency f_{RO} across temperatures. Figure 9 shows f_{RO}

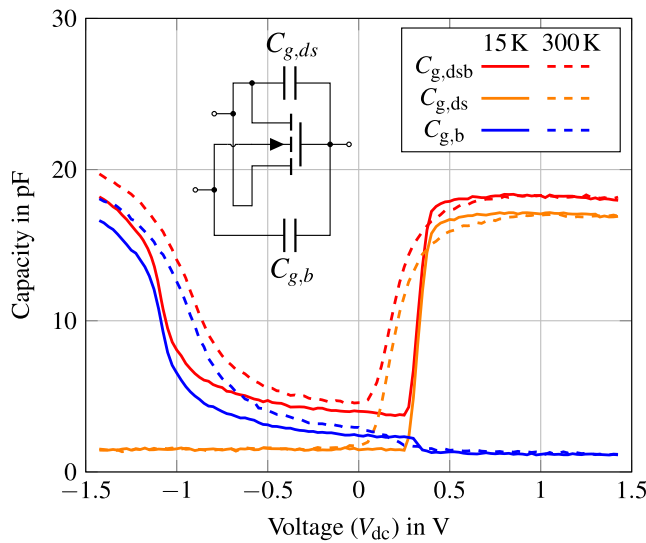


FIG. 10. CV-curve of 1000 MOSFET devices in parallel at 300 and 15 K at a frequency of 10 kHz. They are p-channel MOSFETs with a width of $0.12\ \mu\text{m}$ and a length of $10\ \mu\text{m}$. The device was measured with one dc probe as outlined in Table II(c).

across supply voltage for a temperature sweep from 300 to 15 K. The output was recorded with an oscilloscope RTB2004 from *Rohde & Schwarz*. In alignment with other findings, a steady increase in the oscillation frequencies is noted toward lower temperatures, which can be mainly attributed to an increase in the mobility of electrons at cryogenic temperatures.³⁵

C. CV measurements

The parasitic capacitances of a semiconductor device can be determined with capacitance–voltage (CV) measurements. The capacitances depend on the specific material's characteristics and the geometric properties of the devices. In Fig. 10, an equivalent circuit of a device including two of the examined capacitances is shown. Capacitance $C_{g,b}$ is measured between the gate and the bulk of the transistor, while the other capacitance $C_{g,ds}$ is measured between the gate and the combined drain-source connection. A combination of both capacitances is also measured by shorting drain, source, and bulk. This capacitance $C_{g,dsb}$ is equal to the sum of the other capacities,

$$C_{g,dsb} = C_{g,ds} + C_{g,b}. \quad (3)$$

In this setup, a lock-in amplifier is used both as a signal source and a measurement device. It can produce both an ac small signal and a dc bias. For the shown measurements, an ac signal of 10 mV at 10 kHz is used, and the dc bias can be swept between –10 and 10 V. Additional biases can be applied with the above-mentioned SMUs. The limit of detection for this setup is 1 pF. The intrinsic capacitance of the cables between the lock-in amplifier and the DUT is in the range of 30 and 200 pF, depending on the exact measurement setup. This can be compensated by calibrating the measurement with an open measurement.

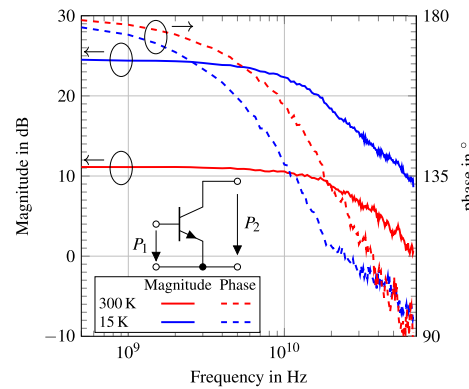


FIG. 11. S-parameter (S_{21}) measurements of a HBT transistor at temperatures of 300 and 15 K. The bias point was chosen at $I_b \approx 2\ \text{mA}$. The device was measured with two GSG probes as outlined in Table II(b).

The device presented in Fig. 10 was measured in a dc bias range of –1.5 to 1.5 V at 300 and 15 K. A shift in the threshold voltage and a lower capacitance in the accumulation and depletion region can be observed. In addition, the sum of $C_{g,b}$ and $C_{g,ds}$ agrees with the measured value for $C_{g,dsb}$ at both temperatures.

D. S-parameters

Frequency-dependent measurements are important for developing integrated circuits. They can be obtained using vector network analyzers. VNAs measure the amplitude and phase of reflected and transmitted waves in a network. In this study, multiple heterojunction npn bipolar transistors (HBTs) from *Infineon* were investigated using an E8361A PNA from *Agilent Technologies*. The transistors were measured over a temperature range from 300 to 15 K.

As this is a 2-port network, two GSG probes were used. The probes were calibrated at each temperature using a short-open-load-through (SOLT) calibration with the CSR-9 calibration substrate from *FormFactor*. Instead of performing the calibration on the VNA, the raw data were recorded, and the calibration was performed afterward using the open-source toolkit *scikit-rf* in *Python*. In addition, open and short de-embedding was performed with this toolkit to remove the influence of the pads and traces on the transistor.

Figure 11 shows a calibrated and de-embedded S-parameter measurement of an npn-transistor up to 67 GHz. The increase in the S_{21} -parameter can be clearly observed and increases toward lower temperatures at the same bias point. One important metric for transistors is their small-signal current gain, which is frequency-dependent. The frequency at which the current gain reaches unity is called the transit frequency f_T . This can be calculated with Eq. (4),³⁶ where f_0 is the evaluation frequency, in this case 10 GHz, and Y_{11}, Y_{21} are the entries of the admittance matrix derived from the S-parameters. In further measurements, the HBT's transit frequency f_T has been measured across temperatures. An exemplary plot of f_T across the HBT's collector currents I_c is shown in Fig. 12. It is evident that the peak f_T increases with lower temperatures and very slightly shifts toward higher I_c .^{37,38} Only a slight

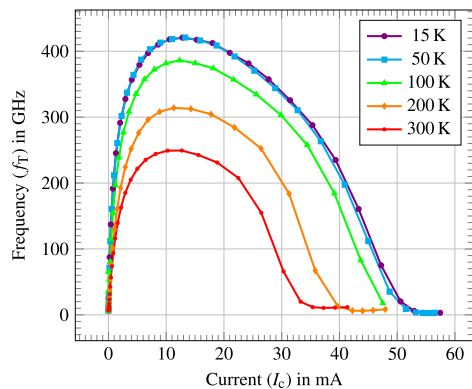


FIG. 12. Temperature-dependent measurement of the extrapolated f_T over I_c at $f_0 = 10$ GHz for a high-speed npn transistor in a BEBC configuration with a $0.19 \times 2.8 \mu\text{m}^2$ drawn emitter size. Measured at an input power of -30 dBm and sweeping V_{ce} and V_{be} synchronously with no offset. The device was measured with two GSG probes as outlined in Table II(b).

increase in f_T from 50 to 15 K can be observed. However, this is in agreement with³⁹ where a f_T saturation below 70 K was also observed,

$$f_T = \frac{f_0}{\Im(Y_{11}/Y_{21})}. \quad (4)$$

E. Integrated CMOS measurements

Scaling integrated trapped-ion quantum computers to large qubit numbers requires independent, highly precise dc control signals to shuttle and confine ions within the surface ion trap.⁴⁰ Developing a shuttling controller system on chip (SoC) that could generate the required voltages next to the quantum processing unit could provide a feasible path to a scalable system.²³ For this purpose, digital-to-analog converters (DACs), capable of generating the required waveforms, have to be developed. A 12 bit

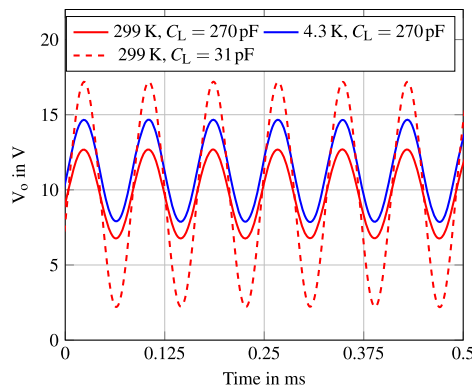


FIG. 13. Measured sinusoidal output at $f_{out} \approx 12.3$ kHz of the 12 bit DAC, operating with an SPI clock frequency of 50 MHz at different capacitive loads of $31 \mu\text{F}$ (short cables and open vacuum chamber) and $270 \mu\text{F}$ (cryogenic configuration). The DUT was mounted directly under the cryocooler as outlined in Table II(e).

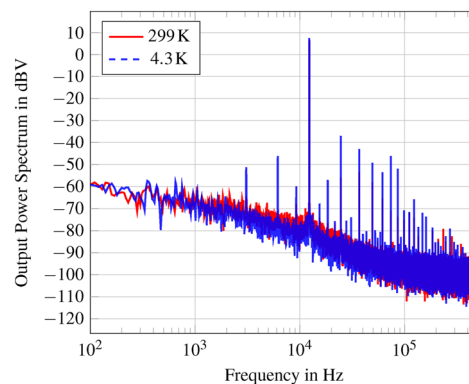


FIG. 14. Evaluated voltage spectrum of the DAC's sinusoidal output at $f_{out} \approx 12.3$ kHz with an effective noise bandwidth (ENBW) of 20.04 Hz, sampling rate of 1 MSa/s, and Blackman-Harris window function. The DUT was mounted directly under the cryocooler as outlined in Table II(e).

DAC^{5,41} was investigated at room and cryogenic temperatures. The DAC chip was glued with conductive silver on an electroless nickel immersion gold (ENIG)-finished carrier PCB and mounted directly at the second stage of the cryocooler, as presented in Table II(e). The temperature was measured on the PCB and reached a final temperature of 4.3 K due to heat dissipation of the DAC during operation. Various supply and reference voltages were supplied, including the main supply voltage for the analog and digital parts of the DAC. The digital part of the DAC includes a 50 MHz serial peripheral interface (SPI), which is used to control the DAC's output voltage. The output of the DAC is single-ended and features a high-voltage output with a full-scale range of up to 17 V.

The output of the DAC was measured using a semi-rigid 0.086 inch coaxial cable with SMA connectors, which was thermalized on the upper stage of the cryocooler. This ensures good thermal conductivity and much better signal integrity than the cryoloop cables. The cryoloop has a lower thermal conductivity, minimizing the thermal loading in the second stage. It was used to supply the voltages to the DAC but also for the digital signals of the SPI interface. A MXO44 oscilloscope from Rohde & Schwarz was used to record the output waveforms.

A sinusoidal waveform at different temperatures and capacitive loads C_L is shown in Fig. 13. Due to the additional capacitive loading of the SMA cables in the vacuum chamber, the measured output amplitude is dramatically affected when conducting measurements inside the cryostat. The same measurement was repeated at 300 K, but with very short cables and an open vacuum chamber, lowering the capacitive load to $C_L = 31 \mu\text{F}$. The corresponding output spectrum of the sinusoidal waveform at $f_{out} \approx 12.3$ kHz, visualized in Fig. 14, shows a slight deterioration of the DAC's performance at cryogenic temperature. Such change contributes to a decrease in the DAC's linearity at cryogenic temperature.

V. CONCLUSION

In this work, a cryogenic measurement platform for the precise characterization of electrical components was presented. The

setup achieves chip-level temperatures as low as 4.2 K, highlighting its suitability for applications in quantum computing and cryogenic semiconductor technologies. It facilitates a broad spectrum of measurements, including dc and frequency-dependent capacitance characterizations, as well as high-frequency two-port S-parameter measurements up to 67 GHz, enabling comprehensive analysis of various semiconductor devices.

The system's versatility is further demonstrated by its capacity to accommodate various probe configurations and incorporate up to 24 twisted-pair control and supply connections. The integration of an optical microscope with machine vision algorithms enhances precision, supporting semi-automated and repeatable probe placement. In addition, the large vacuum chamber and modular design provide the flexibility to interface with a wide range of sample types, from passive components to fully integrated circuits.

In conclusion, this versatile system provides a valuable tool for advancing research in quantum computing and cryogenic electronics, offering high precision and wide-ranging capabilities for testing complex circuits at cryogenic temperatures.

ACKNOWLEDGMENTS

This work was supported in part by the Braunschweig International Graduate School of Metrology (B-IGSM), in part by the Laboratory for Emerging Nanometrology (LENA), in part by the Deutsche Forschungsgemeinschaft (DFG, German Research Foundation) under Germany's Excellence Strategy-EXC-2123 QuantumFrontiers-390837967, in part by the Volkswagen Foundation and the Ministry of Science and Culture of Lower Saxony through "Quantum Valley Lower Saxony Q1" (QVLS-Q1), in part by the BMBF in the project 13N16132 "ATIQ," and in part by the BMBF in a subcontract of 13N15930 in the project "QuMIC." In addition, the authors would like to thank Klaus Auffinger for the technical discussions. Corresponding author: Paul J. Ritter (email: p.ritter@tu-braunschweig.de).

AUTHOR DECLARATIONS

Conflict of Interest

The authors have no conflicts to disclose.

Author Contributions

P. J. Ritter: Conceptualization (supporting); Data curation (lead); Investigation (lead); Methodology (equal); Project administration (supporting); Software (supporting); Validation (equal); Visualization (lead); Writing – original draft (lead); Writing – review & editing (equal). **M.-A. Tucholke:** Data curation (supporting); Investigation (supporting); Software (lead); Validation (equal); Visualization (supporting); Writing – original draft (supporting); Writing – review & editing (equal). **M. Neumann:** Data curation (supporting); Investigation (supporting); Software (supporting); Validation (equal); Visualization (supporting); Writing – original draft (supporting); Writing – review & editing (equal). **J. F. Mumme:** Investigation (supporting); Methodology (supporting); Validation (equal); Writing – original draft (supporting); Writing – review &

editing (equal). **A. Meyer:** Data curation (supporting); Investigation (supporting); Resources (supporting); Validation (supporting); Visualization (supporting); Writing – review & editing (equal). **R. Roederer:** Methodology (supporting); Resources (supporting); Validation (supporting); Writing – review & editing (equal). **Z. Guo:** Data curation (supporting); Resources (supporting); Validation (supporting); Writing – review & editing (equal). **A. Pawlak:** Methodology (supporting); Project administration (supporting); Resources (supporting); Supervision (supporting); Validation (supporting); Writing – review & editing (equal). **V. Issakov:** Funding acquisition (supporting); Project administration (supporting); Resources (supporting); Supervision (supporting); Writing – review & editing (equal). **M. Schilling:** Conceptualization (equal); Funding acquisition (equal); Methodology (supporting); Project administration (equal); Resources (equal); Supervision (equal); Writing – review & editing (equal). **B. Hampel:** Conceptualization (equal); Formal analysis (supporting); Funding acquisition (equal); Methodology (supporting); Project administration (equal); Resources (equal); Supervision (equal); Writing – review & editing (equal).

DATA AVAILABILITY

The data that support the findings of this study are available from the corresponding author upon reasonable request.

REFERENCES

- ¹J. Chiaverini and J. M. Sage, "Insensitivity of the rate of ion motional heating to trap-electrode material over a large temperature range," *Phys. Rev. A* **89**, 012318 (2014).
- ²C. D. Bruzewicz, J. Chiaverini, R. McConnell, and J. M. Sage, "Trapped-ion quantum computing: Progress and challenges," *Appl. Phys. Rev.* **6**, 021314 (2019).
- ³X. Xue, B. Patra, J. P. G. van Dijk, N. Samkharadze, S. Subramanian, A. Corra, B. Paquelet Wuetz, C. Jeon, F. Sheikh, E. Juarez-Hernandez, B. P. Esparza, H. Rampurawala, B. Carlton, S. Ravikumar, C. Nieva, S. Kim, H.-J. Lee, A. Sammak, G. Scappucci, M. Veldhorst, F. Sebastian, M. Babaie, S. Pellerano, E. Charbon, and L. M. K. Vandersypen, "CMOS-based cryogenic control of silicon quantum circuits," *Nature* **593**, 205–210 (2021).
- ⁴J. Jeong, S. K. Kim, Y.-J. Suh, J. Lee, J. Choi, J. P. Kim, B. H. Kim, J. Park, J. Shim, N. Rheem, C. J. Lee, Y. Jo, D.-M. Geum, S.-Y. Park, J. Kim, and S. Kim, "Cryogenic III-V and Nb electronics integrated on silicon for large-scale quantum computing platforms," *Nat. Commun.* **15**, 10809 (2024).
- ⁵A. Meyer, P. Toth, A. Engelhardt, J. Repp, M. Brand, and V. Issakov, "A 12 bit R-2R digital-to-analog converter for shuttling operation in a trapped-ion quantum computer," in *2023 IEEE BiCMOS and Compound Semiconductor Integrated Circuits and Technology Symposium (BCICTS)* (IEEE, 2023), pp. 28–31.
- ⁶G. Kiene, S. İlik, L. Mastrodomenico, M. Babaie, and F. Sebastian, "Cryogenic characterization of low-frequency noise in 40-nm CMOS," *IEEE J. Electron Devices Soc.* **12**, 573–580 (2024).
- ⁷P. A. T Hart, M. Babaie, A. Vladimirescu, and F. Sebastian, "Characterization and modeling of self-heating in nanometer bulk-CMOS at cryogenic temperatures," *IEEE J. Electron Devices Soc.* **9**, 891–901 (2021).
- ⁸H.-C. Han, F. Jazaeri, A. D'Amico, Z. Zhao, S. Lehmann, C. Kretzschmar, E. Charbon, and C. Enz, "Cryogenic RF characterization and simple modeling of a 22 nm FDSOI technology," in *ESSDERC 2022—IEEE 52nd European Solid-State Device Research Conference (ESSDERC)* (IEEE, 2022), pp. 269–272.
- ⁹FormFactor, Inc., HPD IQ3000 Fully Automated Cryogenic Wafer Probing at 4 K, 2023.
- ¹⁰J. T. West, A. Kurlej, A. Wynn, C. Rogers, M. A. Gouker, and S. K. Tolpygo, "Automatic 4 K cryogenic probe station for DC and microwave measurements

- on 150-mm and 200-mm wafers,” in *2022 IEEE/MTT-S International Microwave Symposium—IMS 2022* (IEEE, 2022), pp. 237–240.
- ¹¹ Advanced Research Systems, Inc., PS-CC Closed Cycle Cryogenic Probe Station.
- ¹² Lake Shore Cryotronics, Inc., CRX-4K cryogenic probe station.
- ¹³ D. Russell, K. Cleary, and R. Reeves, “Cryogenic probe station for on-wafer characterization of electrical devices,” *Rev. Sci. Instrum.* **83**, 044703 (2012).
- ¹⁴ G. J. Höfer, F. Jäger, and H. A. Kratz, “Broadband four-channel cryogenic wafer probing system for automated coplanar on-chip measurements,” *Rev. Sci. Instrum.* **64**, 788–792 (1993).
- ¹⁵ Y. Kudabay, P. J. Ritter, and V. Issakov, “A single-stage 24 Gb/s 8:1 cryogenic multiplexer for Josephson arbitrary waveform synthesizer,” in *2024 IEEE BiCMOS and Compound Semiconductor Integrated Circuits and Technology Symposium (BCICTS)* (IEEE, 2024), pp. 58–61.
- ¹⁶ M. Tollkühn, P. J. Ritter, M. Schilling, and B. Hampel, “THz microscope for three-dimensional imaging with superconducting Josephson junctions,” *Rev. Sci. Instrum.* **93**, 043708 (2022).
- ¹⁷ B. Hampel, M. Tollkühn, I. Elenskiy, M. Martens, D. Kajevic, and M. Schilling, “Josephson cantilevers for THz microscopy of additive manufactured diffractive optical components,” *IEEE Trans. Appl. Supercond.* **29**, 1800304 (2019).
- ¹⁸ P. J. Ritter, F.-N. Stapelfeldt, M. Tollkühn, D. Hanisch, M. Pröpper, M. Schilling, and B. Hampel, “Antenna designs for efficient coupling to Josephson junctions for THz microscopy,” *IEEE Trans. Appl. Supercond.* **33**, 1800705 (2023).
- ¹⁹ A. Chijioke and J. Lawall, “Vibration spectrum of a pulse-tube cryostat from 1 Hz to 20 kHz,” *Cryogenics* **50**, 266–270 (2010).
- ²⁰ T. Tomaru, T. Suzuki, T. Haruyama, T. Shintomi, A. Yamamoto, T. Koyama, and R. Li, “Vibration analysis of cryocoolers,” *Cryogenics* **44**, 309–317 (2004).
- ²¹ R. C. Dhuley, M. Ruschman, J. T. Link, and J. Eyre, “Thermal conductance characterization of a pressed copper rope strap between 0.13 K and 10 K,” *Cryogenics* **86**, 17–21 (2017).
- ²² L. Enthoven, J. van Staveren, J. Gong, M. Babaie, and F. Sebastian, “A 3 V 15b 157 μ W cryo-CMOS DAC for multiplexed spin-qubit biasing,” in *2022 IEEE Symposium on VLSI Technology and Circuits (VLSI Technology and Circuits)* (IEEE, 2022), pp. 228–229.
- ²³ J. Stuart, R. Panock, C. d. Brzewicz, J. A. Sedlacek, R. McConnell, I. L. Chuang, J. M. Sage, and J. Chiaverini, “Chip-integrated voltage sources for control of trapped ions,” *Phys. Rev. Appl.* **11**, 024010 (2019).
- ²⁴ P. Vliex, C. Degenhardt, C. Grewing, A. Kruth, D. Nielinger, S. van Waasen, and S. Heinen, “Bias voltage DAC operating at cryogenic temperatures for solid-state qubit applications,” *IEEE Solid-State Circuits Lett.* **3**, 218–221 (2020).
- ²⁵ S. K. Nayar and Y. Nakagawa, “Shape from focus,” *IEEE Trans. Pattern Anal. Mach.* **16**, 824–831 (1994).
- ²⁶ N. K. El Abbadi, S. A. Al Hassani, and A. H. Abdulkhaleq, “A review over panoramic image stitching techniques,” *J. Phys.: Conf. Ser.* **1999**, 012115 (2021).
- ²⁷ R. Hartley and A. Zisserman, *Multiple View Geometry in Computer Vision*, 2nd ed. (Cambridge University Press, 2004).
- ²⁸ L. Zhao and Z. Zhang, “A improved pooling method for convolutional neural networks,” *Sci. Rep.* **14**, 1589 (2024).
- ²⁹ A. Beckers, F. Jazaeri, A. Ruffino, C. Bruschini, A. Baschirotto, and C. Enz, “Cryogenic characterization of 28 nm bulk CMOS technology for quantum computing,” in *2017 47th European Solid-State Device Research Conference (ESSDERC)* (IEEE, 2017), pp. 62–65.
- ³⁰ H. Homulle, L. Song, E. Charbon, and F. Sebastian, “The cryogenic temperature behavior of bipolar, MOS, and DTMOS transistors in standard CMOS,” *IEEE J. Electron Devices Soc.* **6**, 263–270 (2018).
- ³¹ M. A. Zahra, J. Repp, M. Hartmann, M. Brandl, and R. Brederlow, “Evaluation of LDMOS device’s behavior at cryogenic temperatures,” in *2024 International Semiconductor Conference (CAS)* (IEEE, 2024), pp. 181–184.
- ³² M. Sieberer, C. Sandner, and P. Hadley, “A cryogenic high-voltage amplifier for ion traps,” in *SMACD/PRIME 2021; International Conference on SMACD and 16th Conference on PRIME* (IEEE, 2021), pp. 1–4.
- ³³ E. Charbon, F. Sebastian, A. Vladimirescu, H. Homulle, S. Visser, L. Song, and R. M. Incandela, “Cryo-CMOS for quantum computing,” in *2016 IEEE International Electron Devices Meeting (IEDM)* (IEEE, 2016), pp. 13.5.1–13.5.4.
- ³⁴ B. Patra, R. M. Incandela, J. P. G. van Dijk, H. A. R. Homulle, L. Song, M. Shahmohammadi, R. B. Staszewski, A. Vladimirescu, M. Babaie, F. Sebastian, and E. Charbon, “Cryo-CMOS circuits and systems for quantum computing applications,” *IEEE J. Solid-State Circuits* **53**, 309–321 (2018).
- ³⁵ I. V. Vernik, T. A. Ohki, M. B. Ketchen, and M. Bhushan, “Performance characterization of PD-SOI ring oscillators at cryogenic temperatures,” in *2010 IEEE International SOI Conference (SOI)* (IEEE, 2010), pp. 1–2.
- ³⁶ C. C. McAndrew, “On f_T,” in *2015 IEEE Bipolar/BiCMOS Circuits and Technology Meeting—BCTM* (IEEE, 2015), pp. 137–140.
- ³⁷ A. Beckers, F. Jazaeri, and C. Enz, “Characterization and modeling of 28-nm bulk CMOS technology down to 4.2 K,” *IEEE J. Electron Devices Soc.* **6**, 1007–1018 (2018).
- ³⁸ S. Bonen, G. Cooke, T. Jager, A. Bharadwaj, S. P. Tripathi, D. Céli, P. Chevalier, P. Schvan, and S. P. Voinigescu, “Cryogenic characterization of the high frequency and noise performance of SiGe HBTs from DC to 70 GHz and down to 2 K,” *IEEE Microwave Wireless Compon. Lett.* **32**, 696–699 (2022).
- ³⁹ X. Jin, M. Müller, P. Sakalas, A. Mukherjee, Y. Zhang, and M. Schröter, “Advanced SiGe:C HBTs at cryogenic temperatures and their compact modeling with temperature scaling,” *IEEE J. Explor. Solid-State Comput. Devices Circuits* **7**, 175–183 (2021).
- ⁴⁰ S. A. Moses, C. H. Baldwin, M. S. Allman, R. Ancona, L. Ascarrunz, C. Barnes, J. Bartolotta, B. Bjork, P. Blanchard, M. Bohn, J. G. Bohnet, N. C. Brown, N. Q. Burdick, W. C. Burton, S. L. Campbell, J. P. Campora, C. Carron, J. Chambers, J. W. Chan, Y. H. Chen, A. Chernoguzov, E. Chertkov, J. Colina, J. P. Curtis, R. Daniel, M. DeCross, D. Deen, C. Delaney, J. M. Dreiling, C. T. Ertsgaard, J. Esposito, B. Estey, M. Fabrikant, C. Figgatt, C. Foltz, M. Foss-Feig, D. Francois, J. P. Gaebler, T. M. Gatterman, C. N. Gilbreth, J. Giles, E. Glynn, A. Hall, A. M. Hankin, A. Hansen, D. Hayes, B. Higashi, I. M. Hoffman, B. Horning, J. J. Hout, R. Jacobs, J. Johansen, L. Jones, J. Karcz, T. Klein, P. Lauria, P. Lee, D. Liefer, S. T. Lu, D. Lucchetti, C. Lytle, A. Malm, M. Matheny, B. Mathewson, K. Mayer, D. B. Miller, M. Mills, B. Neyenhuis, L. Nugent, S. Olson, J. Parks, G. N. Price, Z. Price, M. Pugh, A. Ransford, A. P. Reed, C. Roman, M. Rowe, C. Ryan-Anderson, S. Sanders, J. Sedlacek, P. Shevchuk, P. Siegfried, T. Skripka, B. Spaun, R. T. Sprenkle, R. P. Stutz, M. Swallows, R. I. Tobey, A. Tran, T. Tran, E. Vogt, C. Volin, J. Walker, A. M. Zolot, and J. M. Pino, “A race-track trapped-ion quantum processor,” *Phys. Rev. X* **13**, 041052 (2023).
- ⁴¹ A. Meyer, Z. Guo, M. Neumann, P. J. Ritter, J. Repp, M. Brandl, M. Schilling, and V. Issakov, “A low-power cryogenic analog electrode signal processing unit for shuttling operations in a trapped-ion quantum computer,” in *2024 IEEE European Solid-State Electronics Research Conference (ESSERC)* (IEEE, 2024), pp. 484–487.